FORM TI-12
07/1999

B-T-3264

FRACTURE TOUGHNESS OF ALLOY 600 AND EN82H WELD IN AIR AND WATER

W. J. Mills and C. M. Brown

U. S. Department of Energy Contract DE-AC11-98PN38206

June 1999

BETTIS ATOMIC POWER LABORATORY WEST MIFFLIN, PENNSYLVANIA 15122-0079

Operated for the U.S. Department of Energy
by Bechtel Bettis, Inc.

DISCLAIMER

DISCLAIMER

Portions of this document may be illegible in electronic image products. Images are produced from the best available original document.

FRACTURE TOUGHNESS OF ALLOY 600 AND EN82H WELD IN AIR AND WATER

W. J. Mills and C. M. Brown

ABSTRACT

The fracture toughness of Alloy 600 and its weld, EN82H, was characterized in 54°C to 338°C air and hydrogenated water. Elastic-plastic J_{IC} testing was performed due to the inherent high toughness of these materials. Alloy 600 exhibited excellent fracture toughness under all test conditions. While EN82H welds displayed excellent toughness in air and high temperature water, a dramatic toughness degradation occurred in water at temperatures below 149°C. Comparison of the cracking response in low temperature water with that for hydrogen-precharged specimens tested in air demonstrated that the loss in toughness is due to a hydrogen-induced intergranular cracking mechanism. At loading rates above ~1000 MPa$\sqrt{m}$/h, the toughness in low temperature water is improved because there is insufficient time for hydrogen to embrittle grain boundaries. Electron fractographic examinations were performed to correlate macroscopic properties with key microstructural features and operative fracture mechanisms.

INTRODUCTION

Alloy 600 and its weld, EN82H, are used in commercial primary water reactors (PWR) where they are exposed to water that can lead to environmental cracking. Alloy 600 components that have failed due to environmental cracking include piping, pressurizer heater sleeve penetrations, instrument nozzles, reactor vessel closure head penetrations, mechanical plugs and steam generator tubes.[1-3] Failure typically involves crack initiation and propagation as a result of stress corrosion cracking (SCC) or corrosion fatigue, followed by stable and unstable tearing when a critical crack size is reached. This study focuses on the final step in the cracking process involving stable and unstable tearing.

While nickel-base alloys such as Alloy 600 and EN82H welds possess excellent toughness in air, a preliminary study[4] indicates that their fracture properties are degraded in low temperature water. Hence, the objective of this study is to characterize the effects of low and high temperature water on the fracture resistance of Alloy 600 and EN82H weld. Fracture properties were characterized using elastic-plastic J_{IC} concepts due to the ductile response exhibited by these materials. Scanning electron microscopy (SEM) examinations of fracture surfaces were performed to correlate trends in fracture toughness behavior with operative cracking mechanisms and key microstructural features. The role of hydrogen embrittlement in degrading fracture properties in the low temperature regime was evaluated by comparing the cracking behavior in low temperature water with that for hydrogen-precharged specimens tested in air.

MATERIALS AND EXPERIMENTAL PROCEDURE

Test Materials

The Alloy 600 test material consisted of a 50.8-mm thick plate annealed at 982°C and air cooled. The EN82H welds were fabricated using a manual gas-tungsten-arc (GTA) weld process to join 25.4 and 50.8 mm thick Alloy 600 plates or 50.8-mm thick plates of Alloy 600 and EN82 clad A516 Grade 70 steel. All plates had a 25° weld prep. Alloy 600 to Alloy 600 welds were full penetration welds (Figures 1a and 1b) and Alloy 600 to clad steel welds were partial penetration welds (Figure 1c). Welds were fabricated by three manufacturers (i.e., "A", "B" and "C") using either a pure argon shield gas (Welds A1, A2, B1, C4 and C5) or a 98%/2% or 95%/5% argon-hydrogen shield gas (Welds C1, C2 and C3) to improve weldability. All welds were tested in the as-welded condition. Chemical compositions and mechanical properties for the test materials are provided in Tables 1 and 2.

Representative microstructures for the test materials are shown in Figure 2. The Alloy 600 plate has a duplex grain size where fine grains with a mean grain diameter of ~20 μm surround isolated unrecrystallized grains with a mean diameter of ~120 μm. Intergranular and intragranular M_7C_3 carbides are observed in both the fine and coarse grain regions and there is evidence of coarse MC-type inclusions. This heat also exhibits a pronounced hot deformation substructure with dislocation subgrains.[5]

The EN82H welds have well-defined grain boundaries separating colonies of similarly oriented dendrites. The grain structure is anisotropic, particularly in the weld root region, where columnar grains are aligned in the transverse direction. Grain boundaries are decorated with fine niobium and titanium-rich MC carbides. Small and intermediate size titanium nitrides are also observed along grain boundaries and in the interdendritic regions.

Fracture Toughness Testing

Fracture tests were performed on precracked compact tension (CT) specimens that had a width (W) of 30.5 mm and thickness (B) of 15.2 mm. All EN82H specimens and most Alloy

600 specimens had 20% side grooves; a few Alloy 600 specimens were not side grooved. Weld specimens were tested in either the longitudinal orientation, with the notch parallel to the welding direction (Figure 1a), or transverse orientation, with the notch normal to the welding direction (Figures 1b and 1c).

Specimens were tested in air and water using servo-electric feedback-controlled systems that were operated in displacement control. Low loading rates, 4 MPa$\sqrt{m}$/h at 54°C and 0.4 to 2 MPa$\sqrt{m}$/h at 338°C, were used to allow sufficient time for environmental effects to occur. Loading rates for a few 54°C water tests were also varied betweeen 0.4 and 26,000 MPa$\sqrt{m}$/h to evaluate rate effects on environmental cracking behavior.

In accordance with multiple-specimen J_{IC} test procedures, specimens were unloaded when the target displacement was reached, heat tinted to discolor the crack extension region, and subsequently fatigued apart so the amount of crack extension (Δa) could be measured by the ASTM E1737-96 nine-point measurement method. Because external load cells were used to measure test load in autoclave tests, the seal friction load was measured and subtracted from the load measurement at the beginning of the test. External linear variable differential transducers (LVDTs) were used to measure external displacement along the load train (v_{LT}), so measured values included displacements due to the load train and specimen compliance. To convert measured load-train displacements to load-line displacements (v_{LL}), the extraneous load-train displacements (due to stretching of the load train and Brinelling of the specimen load-pin holes) must be subtracted out. This was accomplished by comparing the measured compliance ($C_{LT} = \Delta v_{LT}/\Delta P$) in the linear-elastic region with the theoretical load-line compliance ($C_{LL} = \Delta v_{LL}/\Delta P$). The product of instantaneous load and the difference in measured versus theoretical compliances represents the extraneous load-train displacement, which was then subtracted from the load-train displacement to yield the corresponding load-line displacement. The corrected load versus load-line displacement data were used to compute J in accordance with ASTM E1737-96.

The multispecimen J-R curve method was used to establish J_{IC} values, because the periodic unload/reload cycles associated with the unloading compliance method could possibly affect environmental cracking behavior in water. The overall J_{IC} analysis methods were

patterned after ASTM E1737-96. J-R curves were constructed by plotting J values against the corresponding crack extension values (Δa) and fitting the J-Δa data with a power-law regression line. The J_{IC} toughness was then taken to be the value of J at the intersection of the power-law curve with the 0.2 mm offset blunting line:

$$\Delta a = \frac{J}{4\sigma_f} + 0.2 \ (mm) \tag{1}$$

where σ_f is the flow strength, which is equal to the average of the yield and ultimate strength levels [i.e., $\sigma_f = (\sigma_{YS} + \sigma_{UTS})/2$]. Note that the blunting line developed for high strain hardening materials,[6] $J = 4\ \sigma_f\ (\Delta a)$, accurately estimates the apparent blunting behavior for both the wrought and weld metals. Values of the tearing modulus (T), which represents a dimensionless measure of the tearing resistance after J_{IC} is exceeded, were calculated from the following equation:[7]

$$T = \frac{dJ}{da}\frac{E}{\sigma_f^2} \tag{2}$$

where dJ/da is the average slope of the J-R curve (at $\Delta a \approx 1.3$ mm) and E is the elastic modulus. For specimens that exhibited relatively little plasticity prior to the onset of environmental cracking, equivalent critical stress intensity factors (K_{JC}) were computed from experimental J_{IC} values using the equation[8]

$$K_{JC} = \sqrt{E J_{IC}} \tag{3}$$

Although the number and spacing of J-Δa data points do not always conform to ASTM guidelines, the J_{IC} values obtained herein are judged to be accurate estimates of the materials fracture toughness. In cases where insufficient data preclude multispecimen analysis, J-R curves and J_{IC} values were determined using a modified version of the normalization technique proposed by ASTM Task Group E08.08.02. This method estimates crack extension at various points along a load-displacement curve by assuming a unique relationship between load-displacement response and instantaneous crack length. A detailed description of the normalization technique is provided in Reference (9). In this paper, multispecimen and normalized J-R curves are represented by solid and broken lines, respectively.

Test Environment

Flowing autoclaves were used to conduct tests in hydrogenated deaerated water at room temperature, 54°, 93°, 149° and 338°C. Room temperature pH was 10.1 to 10.3 and the oxygen concentration typically ranged between 3 and 17 ppb. The nominal hydrogen concentration was 150 cc H_2/kg H_2O, but ranged from 140 to 180 cc H_2/kg H_2O.

Hydrogen Precharging

Hydrogen precharging was conducted in a high pressure autoclave using 99.999% pure hydrogen. As-fabricated CT specimens were first cleaned in acetone and then rinsed in alcohol before being inserted into the autoclave. To assure a uniform hydrogen distribution, precharging runs were performed at 360°C for 6 weeks. After precharging, the specimens were refrigerated below 0°C to minimize hydrogen loss. Hydrogen concentrations for at least two specimens for each test material were measured after rising load testing was complete. Chips produced by hole drilling were collected for hydrogen analysis. Care was taken not to heat the sample or contaminate the chips. Vacuum extraction analysis on a LECO hydrogen analyzer was performed to measure hydrogen content. The range of hydrogen concentrations was 42 to 45 ppm for Alloy 600 and 55 to 57 ppm for EN82H weld.

Fracture Toughness Testing of Hydrogen-Precharged Specimens

Hydrogen-precharged CT specimens were also tested in 24°C air and water at a nominal $\dot{K}$ of 3 MPa$\sqrt{m}$/h. The resulting load versus load-line displacement curves and maximum stress intensity factors (K_{Pmax}) for these tests are compared with those obtained for non-precharged specimens tested in water to determine if hydrogen embrittlement is responsible for the degraded fracture toughness response in low temperature water. Values of K_{Pmax} were computed by substituting the maximum load and initial crack length into the K solution in ASTM E1737-96. While K_{Pmax} values are not strictly valid when significant plasticity occurs (i.e., >60 MPa$\sqrt{m}$), they provide a relative ranking of susceptiblity to low temperature cracking.

Fractographic Examinations

Broken specimen halves were examined on an SEM to characterize the fracture surface morphology in order to compare operative cracking mechanisms for hydrogen-precharged and non-precharged specimens.

RESULTS AND DISCUSSION

Fracture of Alloy 600

The cracking behavior of Alloy 600 in air and water is summarized in Figure 3. It is seen that the fracture response in air is independent of temperature, so the 24°C and 338°C data were combined into a single J-R curve that yielded a J_{IC} of 415 kJ/m^2 and T of 377. High temperature water has almost no effect on the toughness response, while 54°-149°C water causes a modest toughness reduction. The exceptionally high values in air and high temperature water demonstrate that fracture is not an issue for Alloy 600 under these conditions. While J_{IC} in low temperature water is reduced by 30%, sufficient cracking resistance is retained to avoid fracture concerns. In fact, the load-displacement records in Figure 4a show that Alloy 600 exhibits tremendous plastic deformation capabilities in both low and high temperature water.

The dashed J-R curve in Figure 3 reveals that increasing the displacement rate to 300 mm/h ($\dot{K} \approx$ 26,000 MPa$\sqrt{m}$/h) eliminates most of the environmental effect as there is insufficient time to embrittle the crack tip region. During high rate testing in 54°C water, where the time to maximum load is ~20 seconds, there is a substantial recovery in toughness as J_{IC} increases from 284 to 484 kJ/m^2.

Representative fracture surface morphologies for Alloy 600 tested under various conditions are shown in Figure 5. In 54°C and 338°C air, fracture surfaces have a very ductile appearance with three operative cracking mechanisms (Figure 5a), including primary microvoid coalescence, void sheet formation and shear-stretch formation. The primary dimples are nucleated by broken MC-type inclusions and their growth involves considerable plastic deformation as evidenced by extensive serpentine slip on the walls of the very deep dimples. Void sheet regions, associated with a network of very fine dimples,[10,11] often surround the primary dimples. This mechanism occurs when high shear stresses in the ligaments between primary dimples cause intragranular carbides to decohere from the matrix forming an extremely high density of voids that subsequently coalesce to form steep void sheets. Large portions of the fracture surface also exhibit rather nondescript features, termed shear-stretch features.[4]

This feature also results from high local shear stresses, but occurs when there is a lack of failed particles so conventional microvoid coalescence is precluded. Well-defined slip offsets are typically observed in the shear-stretch regions indicating that this mechanism requires extensive plastic deformation. In addition, the few dimples that form in these regions are shallow and elongated, demonstrating that shear stresses play an important role in creating this fracture surface. The overall appearance of the shear-stretch regions is almost identical to conventional stretch zones that develop ahead of fatigue precracks due to crack tip blunting.

The extensive plastic deformation associated with microvoid coalescence, void sheet and shear-stretch mechanisms accounts for the high J_{IC} fracture toughness. The primary difference between low and high temperature air is considerably more evidence of shear-stretch regions at 640°F. As shown in Figure 5b, Alloy 600 fracture surfaces generated in high hydrogen water were indistinguishable from their air counterparts. The identical fracture surface morphologies in air and water are consistent with the high toughness response observed in both environments.

Fracture of EN82H Weld

In air and high temperature water, EN82H welds exhibit very high fracture toughness in both the longitudinal and transverse orientations, as shown in Figures 6 and 7. For the "A" welds, the cracking response in air is seen to be independent of temperature, so 54° and 338°C data were pooled to establish common J-R curves. Longitudinal weld A1 displays exceptionally high toughness with a J_{IC} of 806 kJ/m^2 in air and 679 kJ/m^2 in 338°C water. Although toughness values for transverse weld A2 are about 30-50% lower, they are still sufficiently high to preclude fracture concerns. Welds manufactured by vendor "C" also display exceptionally high fracture toughness, but less anisotropy than the "A" welds. Values of J_{IC} for the "C" welds range from 731-891 kJ/m^2 in the longitudinal orientation to 638-671 kJ/m^2 in the transverse orientation. These results demonstrate that fracture is not a design or operation concern for EN82H welds in air and high temperature water.

In low temperature water, however, the longitudinal welds (A1, B1 and C1) and the transverse welds (A2, C2, C3 and C4) show a dramatic toughness degradation with J_{IC} and

tearing moduli being reduced by one to two orders of magnitude. In 54°C water, the lowest toughness longitudinal (C1) and transverse (C2, C3, C4) welds have J_{IC} values of 14 and 13, and tearing moduli of 3 and 5. While increasing the water temperature to 93°C has little effect on cracking resistance, further increasing the temperature to 149°C produces a significant recovery. This demonstrates that low temperature crack propagation (LTCP) is only an issue below 149°C.

The load-displacement curves in Figure 8a illustrate the dramatic environmental degradation in 54°C water. In contrast with the exceptionally high ductility observed in 338°C water (which is comparable to that observed in air), the specimens tested in low temperature water display very little ductility as environmental cracking causes premature deviation from linear-elastic behavior. Moreover, welds C2, C3 and C4, which cracked under essentially linear-elastic conditions in 54°C water, showed even less ductility than that for Specimen 1395 (Figure 8a).

Because LTCP in the most embrittled welds was initiated in the linear-elastic regime, K_{JC} values tend to be reasonably consistent with K_{Pmax} values, although there was considerable scatter in the latter. For longitudinal weld C1, the K_{JC} value of 54 MPa$\sqrt{m}$ is near the mean of the K_{Pmax} values, which ranged from 40-77 MPa$\sqrt{m}$, For transverse welds C2, C3 and C4, the K_{JC} value of 52 MPa$\sqrt{m}$ falls in the lower portion of the K_{Pmax} range, 48-77 MPa$\sqrt{m}$. The good agreement between K_{JC} and K_{Pmax} for the most embrittled welds suggests that LTCP tends to initiate at or slightly before maximum load, and linear-elastic fracture mechanics can be used to quantify the limiting response. Thus, the lower-bound K_{Pmax} values of 40 and 48 MPa$\sqrt{m}$ can be used in design and operational analyses.

Figure 9, which summarizes the effect of displacement rate on LTCP behavior, shows that the J-R curve response is essentially rate independent below 1.3 mm/h ($\dot{K}$ < 100 MPa$\sqrt{m}$/h). Within this regime, longer exposure times do not further embrittle the crack tip region. Increasing the rate to 15 mm/h (1300 MPa$\sqrt{m}$/h) provides some improvement in toughness and at 305 mm/h (26,000 MPa$\sqrt{m}$/h) toughness is significantly enhanced. At this rate there is insufficient time to fully embrittle the crack tip region. These results indicate that transient loading events with $\dot{K}$ greater than about 1300 MPa$\sqrt{m}$/h will not cause environmental cracking in low temperature water.

Fractographic studies show that the dramatic toughness degradation in low temperature water is associated with a fracture morphology transition from ductile tearing to intergranular cracking. In air and high temperature water, the ductile tearing behavior in EN82H welds involves a combination of microvoid coalescence and shear-stretch formation regardless of crack orientation, as shown in Figure 10. For the longitudinal orientation, the tremendous amount of plastic deformation required to initiate and grow primary microvoids (Figure 10a) and create shear-stretch regions (Figure 10b) accounts for the exceptionally high J_{IC} and tearing modulus. This is evidenced by the extensive serpentine slip offsets found in all areas of the fracture surface. The fracture resistance for the longitudinal weld was higher than its base metal counterpart because of the lack of large primary MC-type inclusions in the welds. In wrought material, the large inclusions typically fracture after a few percent plastic strain, thereby creating large microvoids ahead of the crack tip. The absence of these large inclusions in welds suppresses microvoid nucleation. Additional energy is then required to nucleate microvoids because the smaller nitrides resist fracture and fail by a decohesion process at much higher strains.

The anisotropy in toughness behavior exhibited by the "A" welds is due to crack propagation along rows of carbides that form a preferred crack path. For transverse weld A2, the fracture surface exhibits both well-defined dimples and shallow dimples that tend to be aligned in the crack growth direction. The alignment occurs because carbide clusters often form in the interdendritic regions that are aligned in the heat flow direction during weld solidification. When properly oriented, the rows of carbides serve as effective microvoid nucleation sites that provide a preferred crack path. The alignment is greatest along the columnar grains in the weld root, which is the region tested in specimens machined from weld A2 (see Figure 1c). While the alignment of carbides in the weld root region accounts for the lower J_{IC} in the transverse orientation, the significant plastic deformation required for microvoid growth and shear-stretch formation accounts for the relatively high J_{IC} value of 350 kJ/m^2 and exceptionally high tearing modulus of 349. The "C" welds show less anisotropy because the center of the weld (see Figure 1b), rather than the weld root, was tested in transverse oriented specimens.

In 54°C water, a fracture mechanism transition from ductile tearing to intergranular cracking dramatically reduces cracking resistance. Figure 11 shows that intergranular cracking is dominant regardless of specimen orientation. The failed grain surfaces are rather smooth and often have an undulating appearance that reflects the dendritic nature of the weld; intermediate size nitrides that pinned grain boundaries are apparent in many regions (Figure 11d). Within some grains, there is

evidence of transgranular faceting along steep walls linking two adjacent intergranular cracks with different elevations. The crystallographic facets are well defined (Figure 11d) and sometimes contain coarse slip offsets. As discussed later, both the intergranular and faceted morphologies can be reproduced in hydrogen-precharged specimens tested in air, thereby demonstrating that these cracking modes are associated with hydrogen embrittlment mechanisms.

The overall fracture surface appearance for specimens tested in 54°C water suggests that intergranular cracking first occurs along the most susceptible grain boundaries. This leaves unbroken ligaments in the wake of the advancing intergranular crack in regions where grain boundaries resist cracking. When the primary crack extends well beyond these ligaments, local stress intensities become large enough to nucleate an alternate faceted cracking mechanism that causes ligament failure.

Low Temperature Cracking Mechanism

The embrittlement displayed by EN82H welds in low temperature water is very similar to that observed in Alloy X-750.[12] Because hydrogen embrittlement of grain boundaries was found to be responsible for rapid cracking of Alloy X-750 in low temperature water, a similar hydrogen-assisted cracking mechanism was suspected for EN82H. To understand the possible role of hydrogen in embrittling the weld metal, CT specimens precharged with 56 ppm hydrogen were tested in room temperature air in an attempt to reproduce the cracking mechanisms and degree of embrittlement observed in low temperature water. Most of the tests were conducted at the same loading rate ($\dot{K} \approx 4$ MPa$\sqrt{m}$/h) used in conventional rising load tests to assure that there was sufficient time for fully developing hydrogen enrichment in the peak triaxial stress region ahead of a crack. In addition, a few hydrogen-precharged specimens were rapidly loaded at a $\dot{K}$ of about 4×10^5 MPa$\sqrt{m}$/h (time to reach maximum load was 1 to 3 seconds) to preclude hydrogen from diffusing and accumulating ahead of the crack. These tests were designed to establish the critical hydrogen level necessary to cause intergranular LTCP. Finally, hydrogen-precharged specimens were tested in 54°C water with 150 cc H_2/kg H_2O to determine if hydrogen from the water combines with hydrogen already present to further embrittle the material. Similar testing of Alloy 600 specimens precharged to 44 ppm hydrogen was also performed in an attempt to understand why the wrought metal resists low temperature embrittlement. Results from the hydrogen precharged studies are given below.

Hydrogen-precharged EN82H

Figure 12 compares K values at maximum load (K_{Pmax}) for hydrogen-precharged and non-precharged specimens tested in air and low temperature water. While K_{Pmax} values higher than 60 MPa$\sqrt{m}$ are not valid per linear-elastic fracture mechanics methodology, they provide a relative ranking of LTCP resistance for comparison purposes.

For non-precharged weld specimens, testing in 54°C water is seen to cause a 50% reduction in K_{Pmax} from 97-103 to 42-60 MPa$\sqrt{m}$. The hydrogen-precharged weld specimen tested in air exhibits a K_{Pmax} of 58 MPa$\sqrt{m}$ which is consistent with the range of values observed for non-precharged specimens tested in water. Moreover, comparison of Figures 8a and 8b show that load-displacement records for the non-precharged specimen tested in water (M1395) and the precharged specimen tested in air (M1585E) are remarkably similar. The overall agreement in K_{Pmax} values and load-displacement curves strongly implicates hydrogen embrittlement as the cause of the inferior cracking resistance in low temperature water.

Fractographic observations provide additional evidence for a hydrogen embrittlement mechanism, as fracture surface morphologies for non-precharged specimens tested in 54°C water (Figure 11) are almost indistinguishable from those for the precharged specimen tested in air (Figure 13). Intergranular cracking is dominant in the precharged specimen, and the smooth, undulating nature of the grain boundary surfaces is consistent with the morphology for LTCP in water. In addition, small islands of transgranular faceting and poorly defined dimples are observed in both environments (Figures 11c and 13b). Some facets have a sharp crystallographic appearance, while others are poorly defined. Figure 13c shows well-defined facets oriented along planar slip bands which suggests that facet formation is associated with localized failure along planar slip bands.

The presence of periodic slip offsets superimposed on the transgranular facets in both the hydrogen-precharged specimen and non-precharged specimen tested in water (Figure 14) provides additional evidence that a hydrogen embrittlement mechanism is active in low temperature water. This observation indicates that hydrogen in the lattice promotes planar slip. Thus, hydrogen appears to play a dual role in degrading cracking resistance; it reduces grain boundary cohesive strength and promotes planar slip which localizes strain concentrations along

grain boundaries. In summary, the presence of hydrogen, regardless of its source, appears to promote intergranular cracking, planar slip and transgranular faceting. While hydrogen-induced planar slip and intergranular cracking have a profound influence on cracking resistance, hydrogen-induced transgranular cracking appears to be less important because this mechanism occurs very late in the cracking process when the ligaments separating large intergranular cracks fail.

The most severe embrittlement occurs when a precharged weld specimen is tested in low temperature water. Comparison of the load-displacement records for Specimens M1590E and M1585E (see Figure 8b) shows that testing in water causes cracking to initiate at lower loads which results in a further reduction in K_{Pmax} to 39 MPa$\sqrt{m}$. Apparently, hydrogen from the water increases the total hydrogen content ahead of a crack which further degrades cracking resistance. In this case hydrogen from the water is added to the precharged hydrogen to severely weaken grain boundaries, fill traps and interact with dislocations. It is also noted that the presence of hydrogen in the water minimizes the loss of precharged hydrogen from the crack tip region. The fracture surface morphologies for the precharged specimens tested in air and water are virtually identical as intergranular cracking is the dominant mechanism in both cases. The only discernable difference is more crystallographic facets in the transgranular islands of the precharged specimen tested in water.

Rapid loading of the precharged weld restores some ductility and increases K_{Pmax} to an intermediate level of 84 MPa$\sqrt{m}$ (Figure 12). Although there is an increase in ductility, the total amount of plastic deformation is much less than that in air or 338°C water, as shown by comparing load-displacement records for Specimens M1392 and M1588E in Figures 8a and 8b. Rapidly loading of the precharged specimens produces a combination of trangranular and intergranular cracking. Significant intergranular cracking is present, but transgranular cracking mechanisms, including dimple rupture and crystallographic faceting, are dominant.

The critical hydrogen concentration required to cause low temperature embrittlement in water can be estimated by comparing the cracking response in the fast and slow tests on hydrogen-precharged specimens. During the rapid loading test where the time to maximum load is about 1 to 2 seconds, the local hydrogen concentration in the lattice is taken to be the

bulk content (56 ppm) because there is insufficient time for hydrogen to diffuse and accumulate ahead of the crack. Thus, rapid test results for the precharged weld shows that a local hydrogen content of 56 ppm causes a substantial decrease in toughness that is associated with some intergranular cracking and faceting; however, higher hydrogen levels are required to induce predominantly intergranular cracking and reduce toughness levels to those associated with LTCP.

A better estimate of the critical local hydrogen concentration required for LTCP can be obtained from the slow test of the precharged weld specimen. During this test, there is sufficient time for hydrogen to diffuse and accumulate in the peak triaxial stress region ahead of the crack tip. The local hydrogen concentration under equilibrium conditions is estimated using the relationship:[13]

$$\frac{C}{C_o} = \exp \frac{\sigma_H \overline{V}}{RT} \qquad (4)$$

where: C = local hydrogen concentration
C_o = bulk hydrogen concentration
σ_H = hydrostatic stress
$\overline{V}$ = partial molar volume of hydrogen in solid solution
R = universal gas constant
T = absolute temperature

$\overline{V}$, defined as the change in volume produced by the addition of 1 gram-mol of hydrogen into the metal, is estimated to be 1.8 cm^3/mol based on lattice parameter measurements for solutions of hydrogen in nickel and other face-centered cubic metals.[14,15] The peak hydrostatic stress is estimated from References (16) and (17), which reported that the maximum normal stress, σ_{YY}, inside the plastic zone is essentially independent of K_I. The effect of increasing K_I is to expand the peak stress over a wider area and locate the peak stress region farther from the crack tip. For materials with extensive strain hardening capabilities, the magnitude of the peak stress is about five times the yield strength. Assuming plane strain conditions, the peak hydrostatic stress is about 50% of the peak normal stress or 2.5 times the yield strength (σ_{YS} $\approx$ 450 MPa). Based on Equation (4), the peak C/C_o ratio at 24°C is 2.3. Thus, the precharged specimen (with 56 ppm hydrogen) showing grain boundary embrittlement has a peak hydrogen concentration on the order of 130 ppm.

Based on the rapid test results, susceptibility to intergranular cracking starts when local hydrogen levels reach ~50 ppm, although this concentration does not fully embrittle grain boundaries. Increasing peak hydrogen concentration to 130 ppm during low rate testing severely embrittles the grain boundaries and produces the same reduction in K_{Pmax} that is observed for non-precharged specimens tested in water. Hence, the critical local concentration required to produce LTCP in EN82H appears to be about 130 ppm, assuming that cracking events nucleate near the peak triaxial stress location. This value is slightly higher than the 50 to 100 ppm hydrogen required to cause LTCP in Alloy X-750.[12] This indicates that Alloy X-750 grain boundaries are slightly more susceptible to hydrogen embrittlement than EN82H grain boundaries.

Hydrogen-precharged Alloy 600

Testing of hydrogen-precharged specimens suggests that the superior LTCP resistance of Alloy 600, relative to EN82H, is attributed to 1) greater resistance to hydrogen pickup and 2) grain boundaries that resist intergranular cracking. These tests show that Alloy 600 is susceptible to hydrogen embrittlement when peak hydrogen concentrations in the lattice reach ~80 ppm; however, the toughness degradation is not as severe as in EN82H and it involves a transgranular cracking mode. Moreover, non-precharged specimens tested in water show no evidence of this embrittlement mechanism, indicating that Alloy 600 tends to pick up relatively little hydrogen from the water. Specific details concerning the precharged specimen behavior is provided below.

While hydrogen-precharging has relatively little effect on K_{Pmax}, as shown in Figure 12, it does significantly degrade the material's ability to plastically deform. Comparison of load-displacement records in Figures 4a and 4b demonstrates that the precharged specimen tested in air (Specimen M1551E) exhibits less total plastic displacement than the non-precharged specimen tested in 54°C water (B60J-1). Thus, a bulk hydrogen concentration of 44 ppm, which corresponds to a peak concentration of ~80 ppm ahead of a crack [per Equation (4)], causes a greater reduction in total plastic deformation than is observed for non-precharged specimens tested in air. The hydrogen-induced loss in ductility is associated with a transgranular faceting mechanism (Figure 15), rather than intergranular cracking. Thus, Alloy 600 grain boundaries are immune to cracking at a peak hydrogen content on the order of 80

ppm for the internal case. On the other hand, this hydrogen level is sufficient to induce a crystallographic faceting mechanism. The absence of faceting on fracture surfaces of non-precharged specimens tested in 54°C water suggests that local hydrogen levels were much less than 80 ppm; hence, Alloy 600 appears to be more resistant to hydrogen pickup than EN82H welds. This is consistent with the observation that precharging under identical conditions produced bulk hydrogen concentrations of 42-45 ppm for Alloy 600 and 55-57 ppm for EN82H. These findings suggest that hydrogen solubility in Alloy 600 is less than that for EN82H welds.

The facets found in precharged Alloy 600 have a very crisp crystallographic appearance and often contain planar slip offsets (Figure 15). There is limited evidence of poorly defined void sheets, but these shallow voids have a faceted appearance. The combination of crystallographic facets and planar slip offsets indicates that hydrogen promotes heterogeneous slip and localized failure along the slip bands, which is consistent with the EN82H behavior. In the welds, this mechanism is usually preempted by intergranular cracking, except in isolated regions that resist grain boundary separation. By contrast, Alloy 600 grain boundaries are immune to cracking, at least at ~80 ppm hydrogen, so the crystallographic faceting mode is dominant.

Testing the precharged specimen in water causes a very slight decrease in both K_{Pmax} from 70 to 66 MPa$\sqrt{m}$ (Figure 12) and total plastic deformation (Figure 4b). Fracture surfaces for the precharged specimens tested in air and water are essentially identical, with the exception of fewer and more poorly defined void sheets in the latter. Apparently, the combined effect of precharged hydrogen and hydrogen from the water is to further promote planar slip and separation along planar slip bands.

Rapid loading of the precharged Alloy 600 specimen increases K_{Pmax} to 89 MPa$\sqrt{m}$ (Figure 12) and restores significant ductility (Specimen M1553E in Figure 4b). The high K_{Pmax} value is consistent with the enhanced toughness observed in ductile materials when subjected to semi-dynamic and dynamic loading rates.[18] Under rapid loading, the precharged specimen exhibits a ductile tearing mophology, consisting of large primary dimples surrounded by void sheets, that is essentially identical to that for non-precharged specimens. Thus, a hydrogen concentration of 44 ppm is insufficient to induce planar slip and a faceted cracking mode. Local hydrogen levels must be increased by diffusion in order to cause a transition to planar slip.

CONCLUSIONS

The fracture toughness behavior of Alloy 600 and EN82H welds was characterized in 54° to 338°C air and hydrogenated water. The results of this study are given below.

1. Alloy 600 displays exceptionally high fracture toughness in air and high temperature water. While low temperature water causes a modest reduction in J_{IC} and tearing modulus, the overall tearing resistance remains high. The superior toughness in air and water, regardless of temperature, demonstrates that fracture is not a design or operational issue for Alloy 600.

2. The high toughness exhibited by Alloy 600 is attributed to the ductile tearing mechanisms that were operative under all test conditions. These mechanisms included microvoid coalescence, void sheet formation and shear-stretch formation.

3. The high fracture toughness exhibited by EN82H welds in air and high temperature water demonstrates that fracture is not a concern under these conditions. Fracture is a concern, however, in low temperature water as J_{IC} values and tearing moduli are reduced by one to two orders of magnitude. Susceptibility to LTCP is only an issue below 149°C.

4. For the most embrittled welds, LTCP initiates near maximum load within the linear-elastic domain; hence, K_{Pmax} values can be used to quantify the limiting response in design and operational assessments. Lower-bound K_{Pmax} values for longitudinal and transverse welds are 40 and 48 MPa$\sqrt{m}$, respectively.

5. Increasing loading rates above 1000 MPa$\sqrt{m}$/h significantly improves the cracking resistance of EN82H welds in low temperature water because there is insufficient time to fully embrittle the material ahead of a crack. At a rate of 26,000 MPa$\sqrt{m}$/h, fracture toughness is fully restored.

6. The dramatic reduction in toughness in low temperature water is associated with a fracture mechanism transition from ductile tearing to intergranular cracking. In air and

high temperature water, tremendous amounts of plastic deformation are required to initiate and grow primary microvoids and create shear-stretch regions. In low temperature water, intergranular cracking is dominant and there are isolated islands of crystallographic faceting.

7. The degree of embrittlement and cracking mechanisms observed in low temperature water were reproduced in hydrogen-precharged specimens tested in air. This demonstrates that LTCP is a hydrogen embrittlement mechanism where hydrogen from the water weakens grain boundaries so they fail at low strain levels and promotes planar slip which localizes strain concentrations along grain boundaries. The critical hydrogen content in the lattice to produce LTCP in EN82H welds is on the order of 130 ppm.

ACKNOWLEDGEMENT

This work was performed under U. S. Department of Energy Contract DE-AC11-98PN38206 with Bettis Atomic Power Laboratory. The authors wish to acknowledge J. R. Suty, J. R Chalfant, S. A. Derry and R. D. Wineland for performing environmental tests and B. J. Whitmore and R. K. Ramaley for performing SEM fractographic examinations. Appreciation is also extended to D. M. Symons for the enlightening discussions.

REFERENCES

(1) P. Saint Paul and G. Slama, "Steam Generator Materials Degradation," Proceedings of the Fifth International Symposium on Environmental Degradation of Materials in Nuclear Power Systems--Water Reactors, ANS, 1992, pp. 39-49.

(2) D. Alter, Y. Robin, M. Pchon, A. Teissier and B. Thorneret, "Stress Corrosion Cracking of Pressurizer Instrumentation Nozzles in the French 1300 MWe Units," Proceedings of the Fifth International Symposium on Environmental Degradation of Materials in Nuclear Power Systems--Water Reactors, ANS, 1992, pp. 661-666.

(3) D. Buisine, F. Cattant, J. Champredonde, C. Pichon, C. Benhamou, A. Gelpi and M. Vaindirlis, "Stress Corrosion Cracking in the Vessel Closure Head Penetrations of French PWR's," Proceedings of the Sixth International Symposium on Environmental Degradation of Materials in Nuclear Power Systems--Water Reactors, TMS, 1993, pp. 845-851.

(4) C. M. Brown and W. J. Mills, "Effect of Water on Mechanical Properties and Stress Corrosion Behavior of Alloy 600, Alloy 690, EN82H Welds and EN52 Welds," Corrosion, 1999, in press.

(5) D. M. Symons, J. P. Foster, and M. G. Burke, "The Relationship Between Observed Stress Corrosion Cracking Fracture Morphology and Microstructure in Alloy 600," Proceedings of the Eighth International Symposium on Environmental Degradation of Materials in Nuclear Power Systems--Water Reactors, ANS, 1997, pp. 237-248.

(6) P. C. Paris, H. Tada, A. Zahoor and H. Ernst, "The Theory of Instability of the Tearing Mode for Elastic-Plastic Crack Growth," Elastic-Plastic Fracture, ASTM STP 668, 1979, pp. 5-36.

(7) W. J. Mills, "On the Relationship Between Stretch Zone Formation and the J Integral for High Strain-Hardening Materials," Journal of Testing and Evaluation, Vol. 9, 1981, pp. 56-62.

(8) J. A. Begley and J. D. Landes, "The J Integral as a Fracture Criterion," Fracture Toughness, Proceedings of the 1971 National Symposium on Fracture Mechanics, Part II, ASTM STP 514, 1972, pp. 1-20.

(9) W. C. Porr and W. J. Mills, "Application of the Normalization Data Analysis Technique for Single Specimen R-Curve Determination," Bettis Atomic Power Laboratory, Report, B-T-3269, February 1999.

(10) H. C. Rogers, "The Effect of Material Variables on Ductility," Ductility, ASM, 1968, pp. 31-61.

(11) T. B. Cox and J. R. Low, Jr., "An Investigation of the Plastic Fracture of AISI 4340 and 18 Nickel--200 Grade Maraging Steels," Metallurgical Transactions, Vol. 5, 1974, pp. 1457-1470.

(12) W. J. Mills, M. R. Lebo and J. J. Kearns, "Hydrogen Embrittlement, Grain Boundary Segregation and Stress Corrosion Cracking of Alloy X-750 in Low and High Temperature Water," Metallurgical and Materials Transactions, 1999, in press.

(13) W. W. Gerberich and Y. T. Chen, "Hydrogen-Controlled Cracking--An Approach to Threshold Stress Intensity," Metallurgical Transactions, Vol. 6A, 1975, pp. 271-278.

(14) B. B. Baranowski, S. Majchrzak and T. B. Flanagan, "The Volume Increase of FCC Metals and Alloys Due to Interstitial Hydrogen Over a Wide Range of Hydrogen Contents," Journal of Physics F: Metal Physics, Vol. 1, 1971, pp. 258-261.

(15) M. L. Wayman and G. C. Smith, "Hydride Formation in Nickel-Iron Alloys," The Journal of Physics and Chemistry of Solids, Vol. 32, 1971, p. 103.

(16) J. R. Rice and M. A. Johnson, "The Role of Large Crack Tip Geometry Changes in Plane Strain Fracture," Inelastic Behavior of Solids, McGraw-Hill, NY, 1970, pp. 641-672.

(17) R. M. McMeeking, "Finite Deformation Analysis of Crack-Tip Opening in Elastic-Plastic Materials and Implications for Fracture," Journal of the Mechanics and Physics of Solids, Vol. 25, 1977, pp. 357-381.

(18) W. J. Mills, "Fracture Toughness of Type 304 and 316 Stainless Steels and Their Welds," International Materials Reviews, Vol. 42, 1997, pp. 45-82.

Table 1 - Material Chemistries (weight percent)									
Mat'l	Alloy 600	EN82H Welds							
Weld ID / Orient.		"B1" Long	"A1" Long	"C1" Long	"A2" Trans	"C2" Trans	"C3" Trans	"C4" Trans	"C5" Long
Heat or Weld	NX585 3G11	Unk	NX4628 DK	NX860 2D	NX462 8DK	NX790 6D	NX812 8D	NX890 6D	NX860 2D
Shield Gas		Ar	Ar	Ar- 2% H_2	Ar	Ar- 5% H_2	Ar- 5% H_2	Ar	Ar
Element									
C	0.08	0.007	0.03	0.043	0.045	0.04	0.039	0.039	0.04
Mn	0.27	2.4	2.39	2.77	2.69	2.80	2.83	2.78	2.77
Fe	8.61	1.5	2.02	1.18	1.53	1.08	0.83	1.34	1.18
S	0.0003	0.0007	<0.001	0.001	0.001	0.003	<0.001	<0.001	0.001
Si	0.25	<0.1	0.087	0.32	0.15	0.069	0.15	0.092	0.32
Cu	0.11	0.06	NM	0.08	0.06	NM	NM	NM	0.08
Ni	73.6	73.2	73.9	72.6	72.1	73.4	73.7	72.2	72.6
Cr	16.08	18.7	19.51	20.3	20.7	20.19	19.58	20.03	20.3
Al	0.16	0.09	NM	0.04	0.07	NM	NM	NM	0.04
Ti	0.41	0.4	0.39	0.29	0.41	0.41	0.33	0.33	0.29
P	0.011	<0.001	<0.001	<0.001	<0.001	<0.001	<0.001	<0.001	<0.001
Nb + Ta	0.121	NM	2.10	2.39	2.35	2.43	2.43	2.39	2.39

NM = Not Measured
Unk = Unknown

Table 2 - Summary of Tensile Test Results										
			EN82H				Alloy 600			
T	Env	Prop	$\bar{x}$	H	L	s	$\bar{x}$	H	L	s
338°C	Water	σ_{YS} (MPa)	397	445	347	30	307	341	259	43
		σ_{UTS} (MPa)	571	622	476	49	661	668	655	7
		%ϵ	32.0	39.0	18.9	6.9	38.9	39.1	38.6	0.3
		%RA	39.1	55.5	23.8	10.3	55.2	56.6	53.0	1.9
54°C	Water	σ_{YS} (MPa)	474	554	373	74	267	323	199	51
		σ_{UTS} (MPa)	601	674	466	70	594	629	527	59
		%ϵ	18.0	27.4	10.1	6.9	34.7	35.6	34.0	0.8
		%RA	27.2	37.8	18.8	7.6	54.4	60.7	43.6	9.4
338°C	Air	σ_{YS} (MPa)	423	489	358	57	288	327	264	34
		σ_{UTS} (MPa)	643	674	599	30	655	666	647	10
		%ϵ	41.5	54.5	25.9	10.3	38.6	39.5	38.1	0.8
		%RA	51.5	54.7	46.1	3.2	56.6	61.6	53.2	4.4
54°C	Air	σ_{YS} (MPa)	436	525	342	63	319	353	292	31
		σ_{UTS} (MPa)	646	679	613	30	654	661	642	10
		%ϵ	34.3	49.1	24.6	9.5	36.5	37.4	35.7	0.9
		%RA	51.2	57.1	37.8	6.7	59.7	64.9	56.2	4.6
RT	Air	σ_{YS} (MPa)	430	483	359	53	337	391	309	47
		σ_{UTS} (MPa)	689	710	680	11	709	714	705	5
		%ϵ	39.6	57.3	23.8	12.9	49.8	50.2	49.5	0.4
		%RA	55.4	58.8	46.7	4.4	62.8	65.7	60.7	2.6

T - test temperature, ENV - test environment,
PROP - material properties: σ_{YS} - yield strength, σ_{UTS} - ultimate strength, %ϵ - percent elongation, %RA - percent reduction in area
$\bar{x}$ - average of all data, H - highest data point, L - lowest data point, s - standard deviation of data

Table 3 - Summary of Fracture Toughness Values for Welds					
Weld	Orient.	Envir.	Temp. (°C)	J_{IC} kJ/m²	T
A1,B1	Long.	Air	54-338	806	364
C5	Long.	Air	24	731; 891	381; 481
A1	Long.	Water	54	42; 60; 79	31; 24; 44
B1	Long.	Water	54	26; 34	18; 15
C1	Long.	Water	54	14	3
C1	Long.	Water	93	19	7
C1	Long.	Water	149	212; 213	84; 118
A1	Long.	Water	338	679	373
A2	Trans.	Air	24-338	350	349
C4	Trans.	Air	24	638; 671	412; 481
A2	Trans.	Water	54	23; 26; 51	26; 13; 35
C2-C4	Trans.	Water	54	13	5
C3	Trans.	Water	149	145; 254	138; 229
A2	Trans.	Water	338	459	245

Long. = Longitudinal Orientation
Trans. = Transverse Orientation

A600JC11

Figure Captions

Figure 1. Orientation of specimens machined from weldments.

Figure 2. Representative microstructures for (a) Alloy 600 and (b) EN82H weld.

Figure 3. J-R curves for Alloy 600 in air and water. Tests in water were conducted at a displacement rate of 0.05 mm/h ($\dot{K}$ = 0.4 MPa$\sqrt{m}$/h) with the exception of one high rate test that was conducted at 300 mm/h ($\dot{K}$ = 24000 MPa$\sqrt{m}$/h).

Figure 4. Load versus load-line displacement curves for Alloy 600. (a) Non-precharged specimens tested in 54° and 338°C water. (b) Hydrogen precharged specimens tested in 24°C air and water. Rapid testing of Specimen M1553E was conducted at a $\dot{K}$ of 4 x 10^5 MPa$\sqrt{m}$/h.

Figure 5. Fracture surface morphology for Alloy 600. (a) 360°C air. Large microvoids surrounded by void sheets (left) and shear stretch region (right). (b) 54°C water. Large microvoids surrounded by void sheets.

Figure 6. J-R curves for EN82H welds with longitudinal orientation tested in air and water. Weld identification is provided inside quotation marks.

Figure 7. J-R curves for EN82H welds with transverse orientation tested in air and water. Weld identification is provided inside quotation marks.

Figure 8. Load versus load-line displacement curves for EN82H weld. (a) Non-precharged specimens tested in 54° and 338°C water. (b) Hydrogen precharged specimens tested in 24°C air and water. Rapid testing of Specimen M1588E was conducted at a $\dot{K}$ of 4 x 10^5 MPa$\sqrt{m}$/h.

Figure 9. Effect of displacement rate on cracking resistance of EN82H weld in 54°C water. Weld identification is provided inside quotation marks.

Figure 10. SEM fractographs of EN82H welds tested in 360°C water. (a) In longitudinal weld specimens, large primary dimples are well defined and often surrounded by void sheets. (b) Longitudinal weld. Equiaxed dimples (right) and shear stretch region (left and center) with elongated dimples and serpentine slip steps. (c) In transverse weld, dimples are sometimes rather shallow and aligned in rows.

Figure 11. SEM fractographs of longitudinal (a) and transverse (b-d) welds tested in 54°C water. (a) (b) Typical intergranular fracture appearance. (c) Typical intergranular cracking with small transgranular region (lower right). (d) High magnification of intergranular fracture (bottom) and transgranular faceting (top).

Figure 12. K_{Pmax} values for EN82H weld and Alloy 600. Non-precharged specimens were tested in 130°F air or water, while hydrogen-precharged [H] specimens were tested in 75°F air or water. The short test times for the rapid loading tests [Rap], where maximum load was reached in 1 to 3 seconds, preclude hydrogen from diffusing to the crack tip; hence, bulk hydrogen levels control fracture behavior. Crosshatching represents a range of K_{Pmax} values.

Figure 13. SEM fractographs of hydrogen-precharged EN82H weld. (a) Intergranular cracking. (b) Intergranular fracture (top and bottom half) surrounding transgranular island with facets and poorly defined dimples. (c) Crystallographic facets within transgranular region.

Figure 14. SEM fractographs of EN82H welds showing planar slip offsets superimposed on transgranular facets. (a) Non-precharged specimen tested in 54°C water. (b) Hydrogen-precharged specimen tested in water.

Figure 15. Fracture surface of hydrogen-precharged Alloy 600 showing slip offsets superimposed on crystallographic facets.

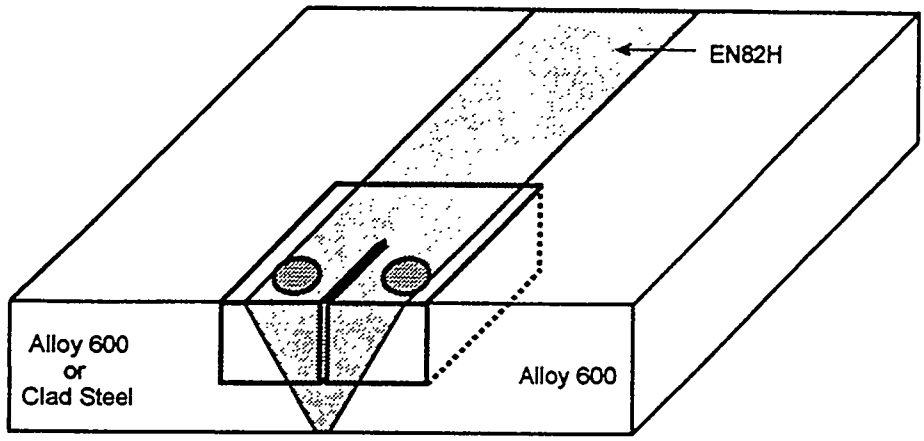

(a) Longitudinal CT

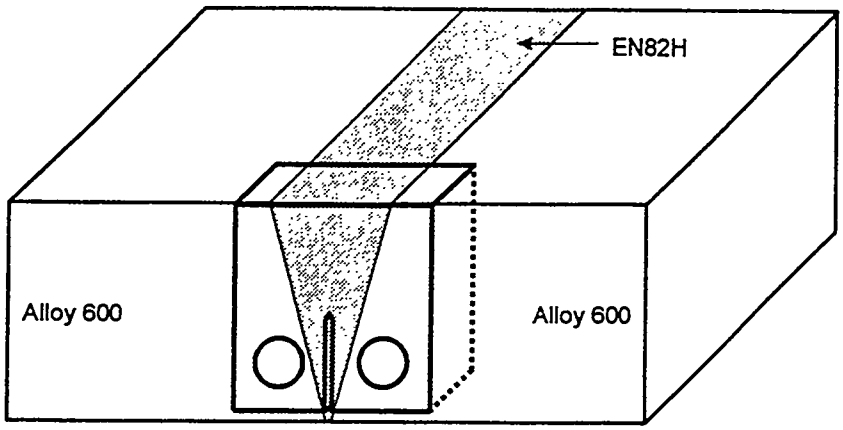

(b) Transverse CT

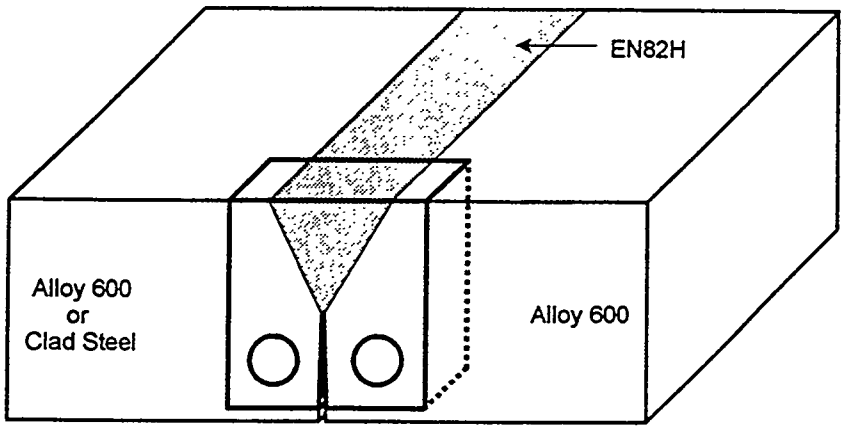

(c) Transverse CT

WLD12.CDR

Figure 1. Orientation of specimens machined from weldments.

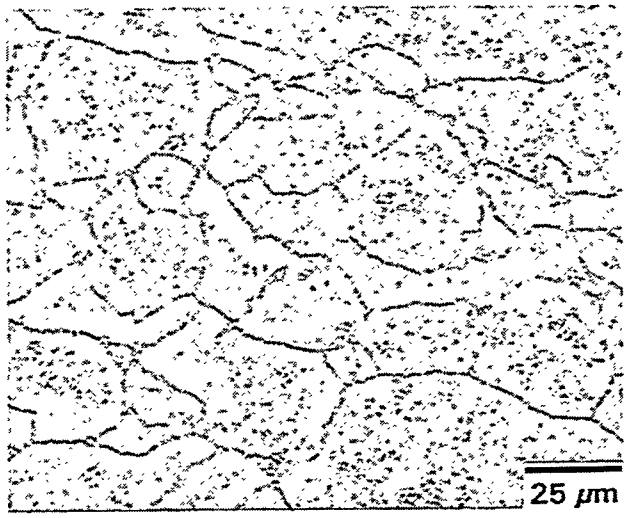

Figure 2. Representative microstructures for (a) Alloy 600 and (b) EN82H weld.

600MIC1d.cdr

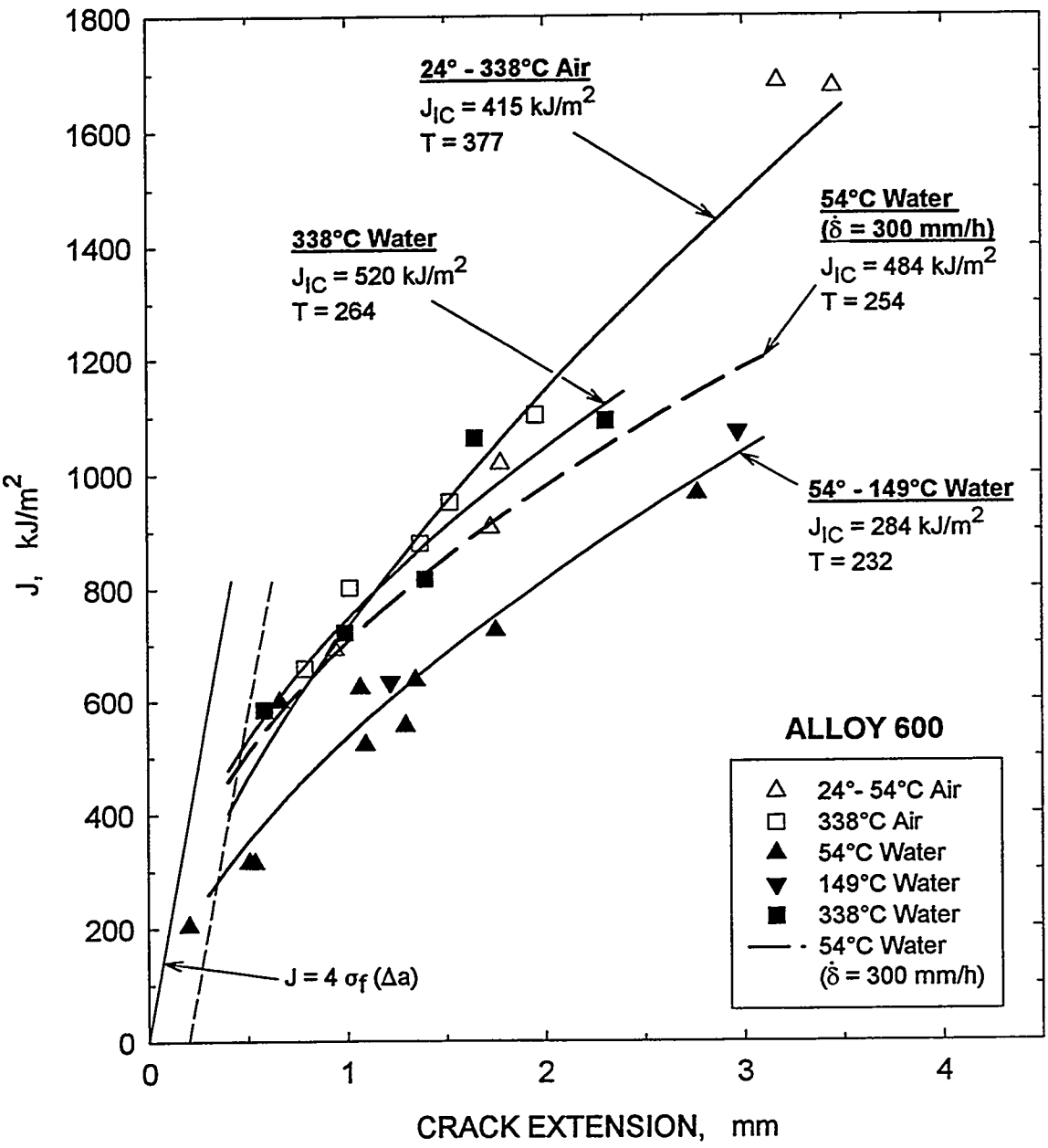

Figure 3. J-R curves for Alloy 600 in air and water. Tests in water were conducted at a displacement rate of 0.05 mm/h ($\dot{K}$ = 0.4 MPa$\sqrt{m}$/h) with the exception of one high rate test that was conducted at 300 mm/h ($\dot{K}$ = 24000 MPa$\sqrt{m}$/h).

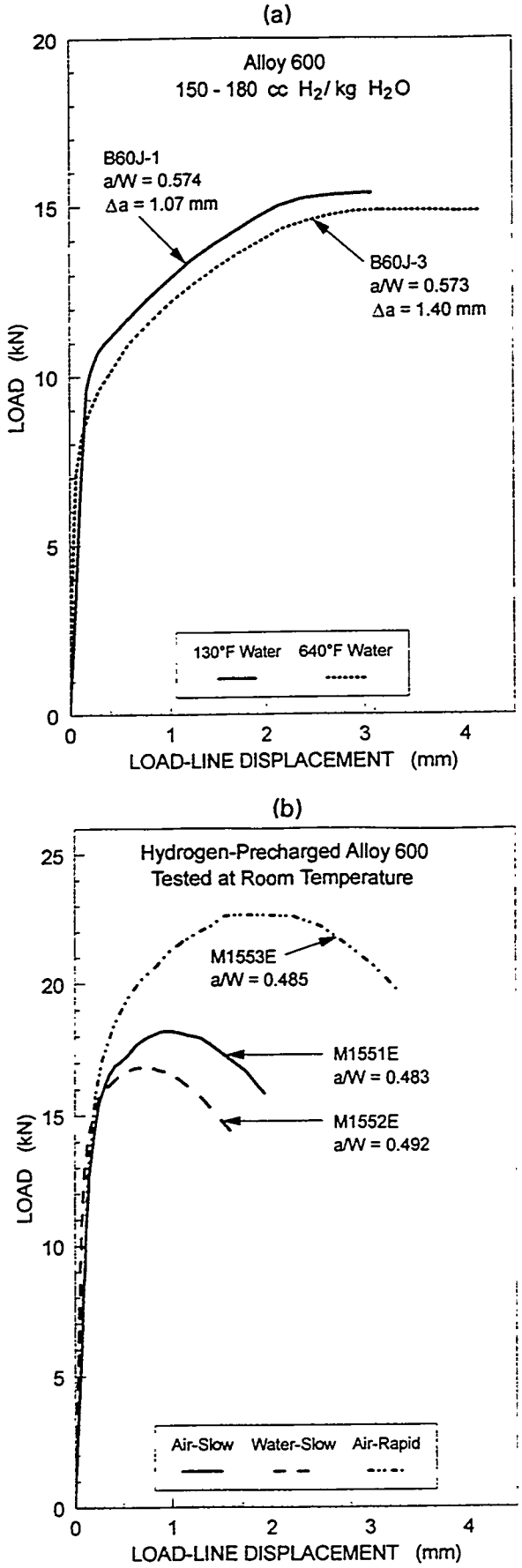

Figure 4. Load versus load-line displacement curves for Alloy 600. (a) Non-precharged specimens tested in 54° and 338°C water. (b) Hydrogen precharged specimens tested in 24°C air and water. Rapid testing of Specimen M1553E was conducted at a $\dot{K}$ of 4 x 10^5 MPa$\sqrt{m}$/h.

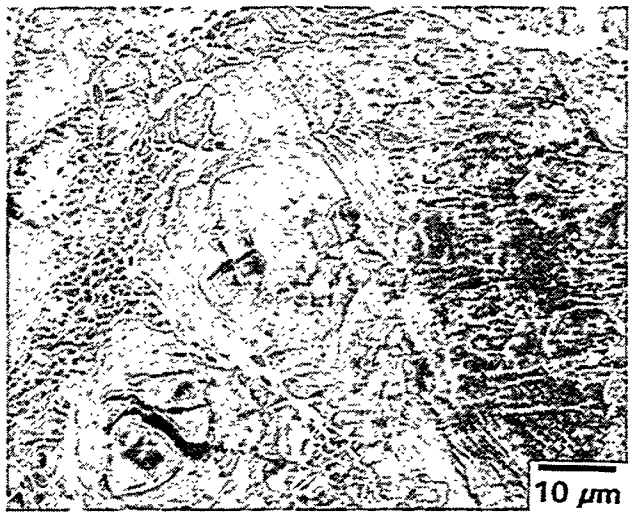

Figure 5. Fracture surface morphology for Alloy 600. (a) 360°C air. Large microvoids surrounded by void sheets (left) and shear stretch region (right). (b) 54°C water. Large microvoids surrounded by void sheets.

600FR11.cdr

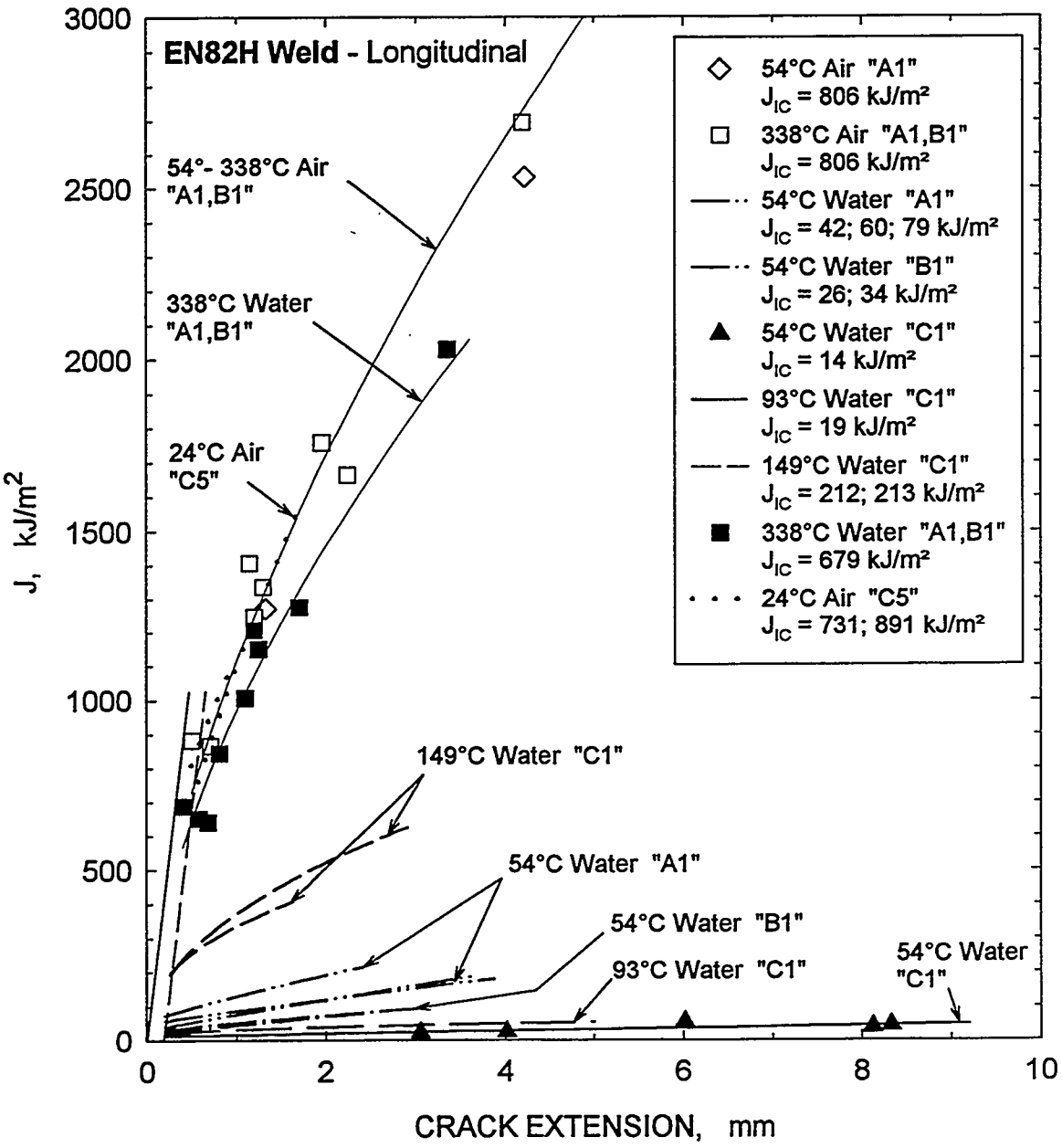

Figure 6. J-R curves for EN82H welds with longitudinal orientation tested in air and water. Weld identification is provided inside quotation marks.

EN82L100

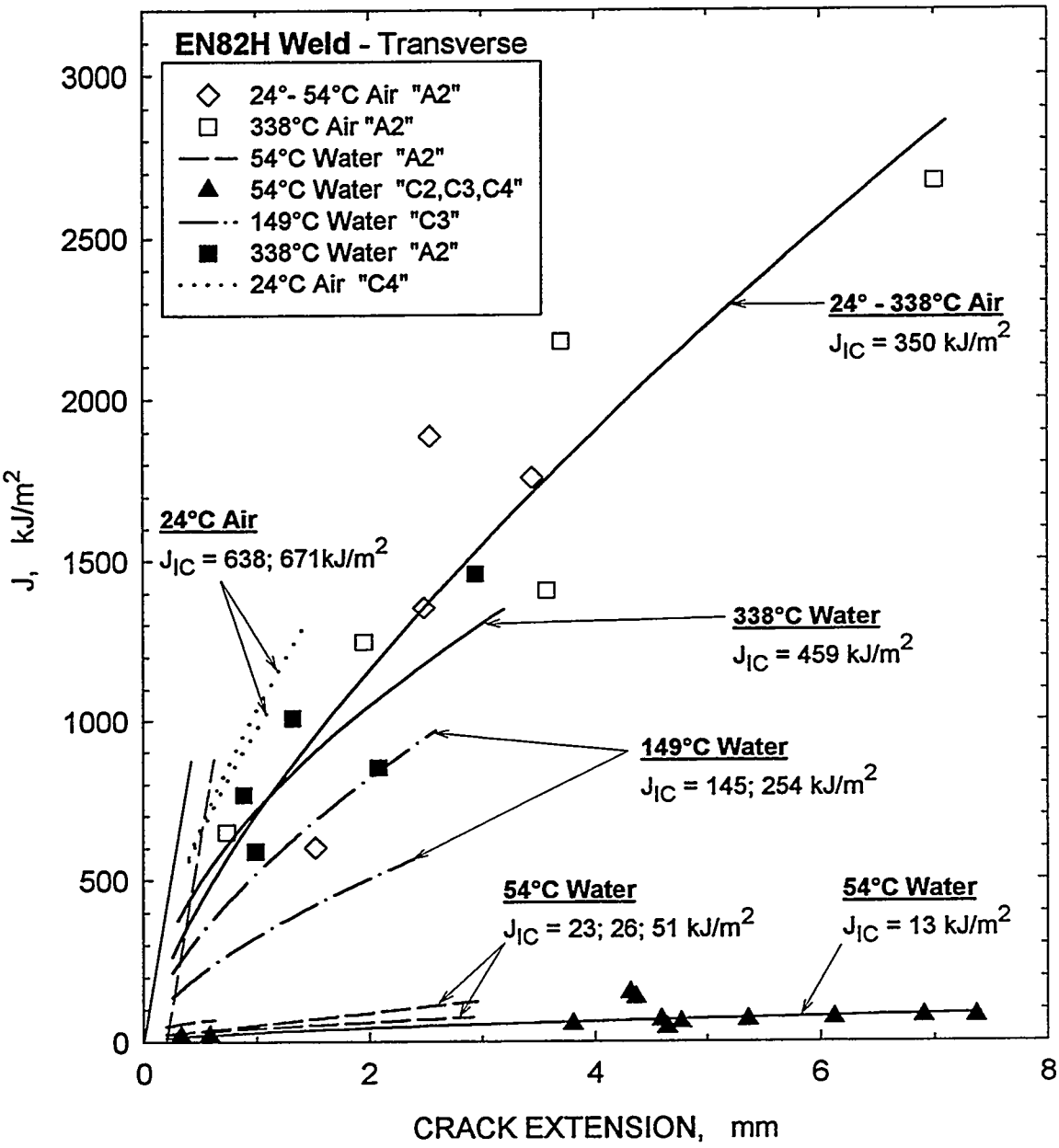

Figure 7. J-R curves for EN82H welds with transverse orientation tested in air and water. Weld identification is provided inside quotation marks.

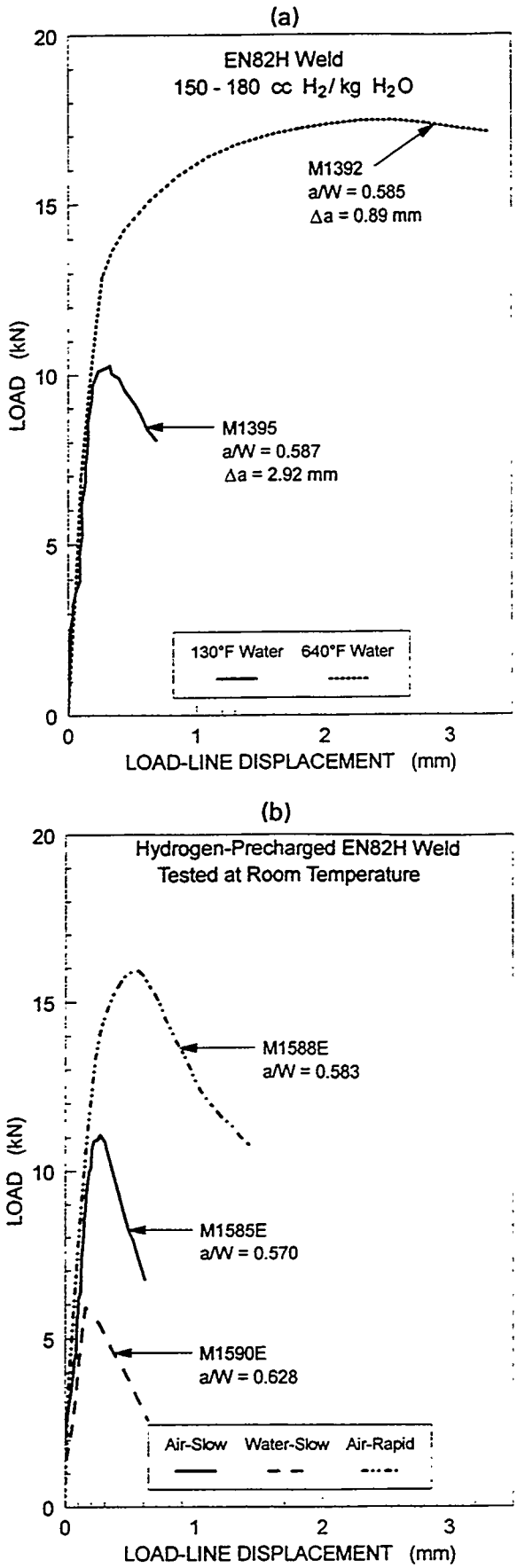

Figure 8. Load versus load-line displacement curves for EN82H weld. (a) Non-precharged specimens tested in 54° and 338°C water. (b) Hydrogen precharged specimens tested in 24°C air and water. Rapid testing of Specimen M1588E was conducted at a $\dot{K}$ of 4 x 10^5 MPa$\sqrt{m}$/h.

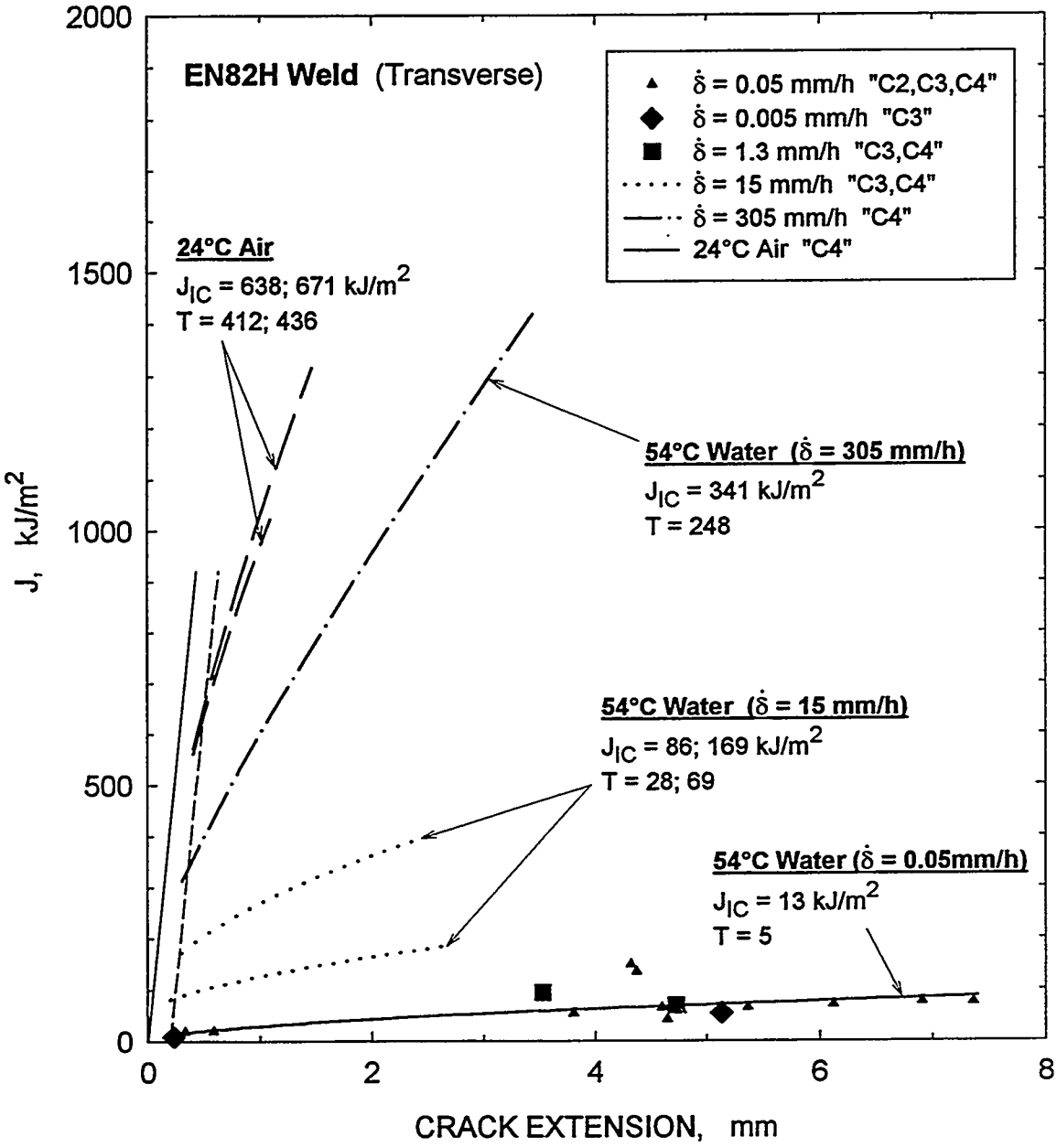

Figure 9. Effect of displacement rate on cracking resistance of EN82H weld in 54°C water. Weld identification is provided inside quotation marks.

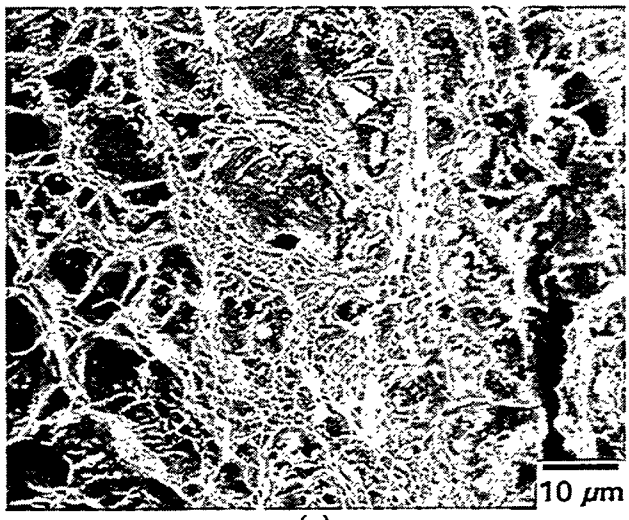

(a)

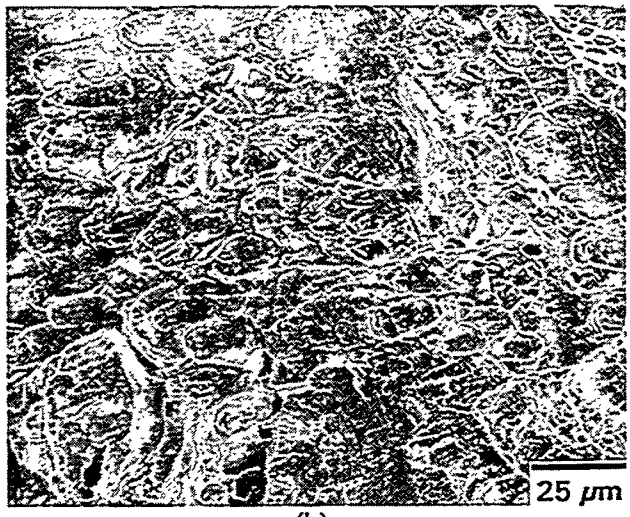

(b)

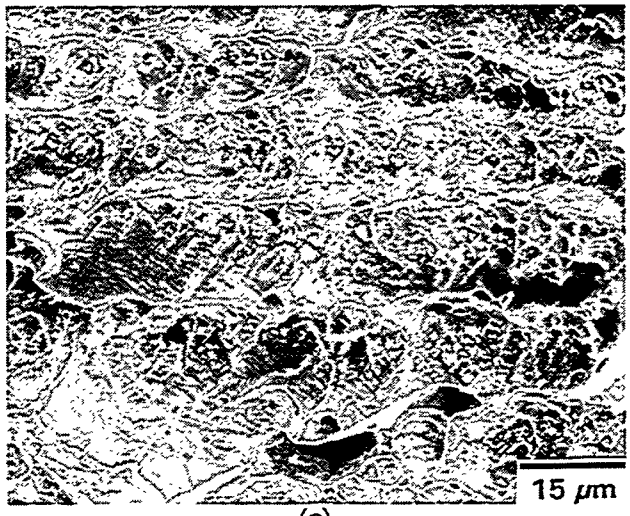

(c)

82FR6a.cdr

Figure 10. SEM fractographs of EN82H welds tested in 360°C water. (a) In longitudinal weld specimens, large primary dimples are well defined and often surrounded by void sheets. (b) Longitudinal weld. Equiaxed dimples (right) and shear stretch region (left and center) with elongated dimples and serpentine slip steps. (c) In transverse weld, dimples are sometimes rather shallow and aligned in rows.

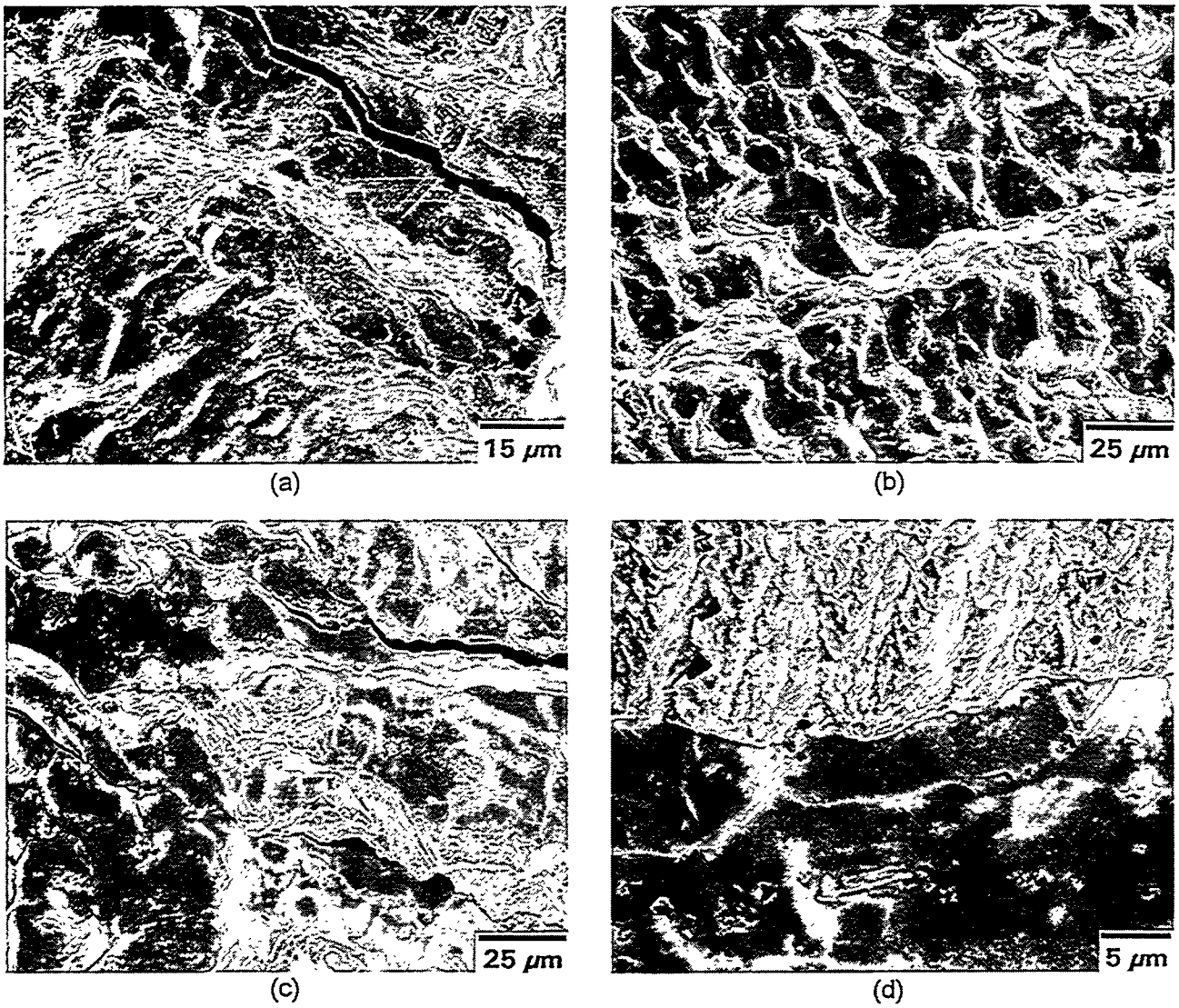

Figure 11. SEM fractographs of longitudinal (a) and transverse (b-d) welds tested in 54°C water. (a) (b) Typical intergranular fracture appearance. (c) Typical intergranular cracking with small transgranular region (lower right). (d) High magnification of intergranular fracture (bottom) and transgranular faceting (top).

82FR5d.cdr

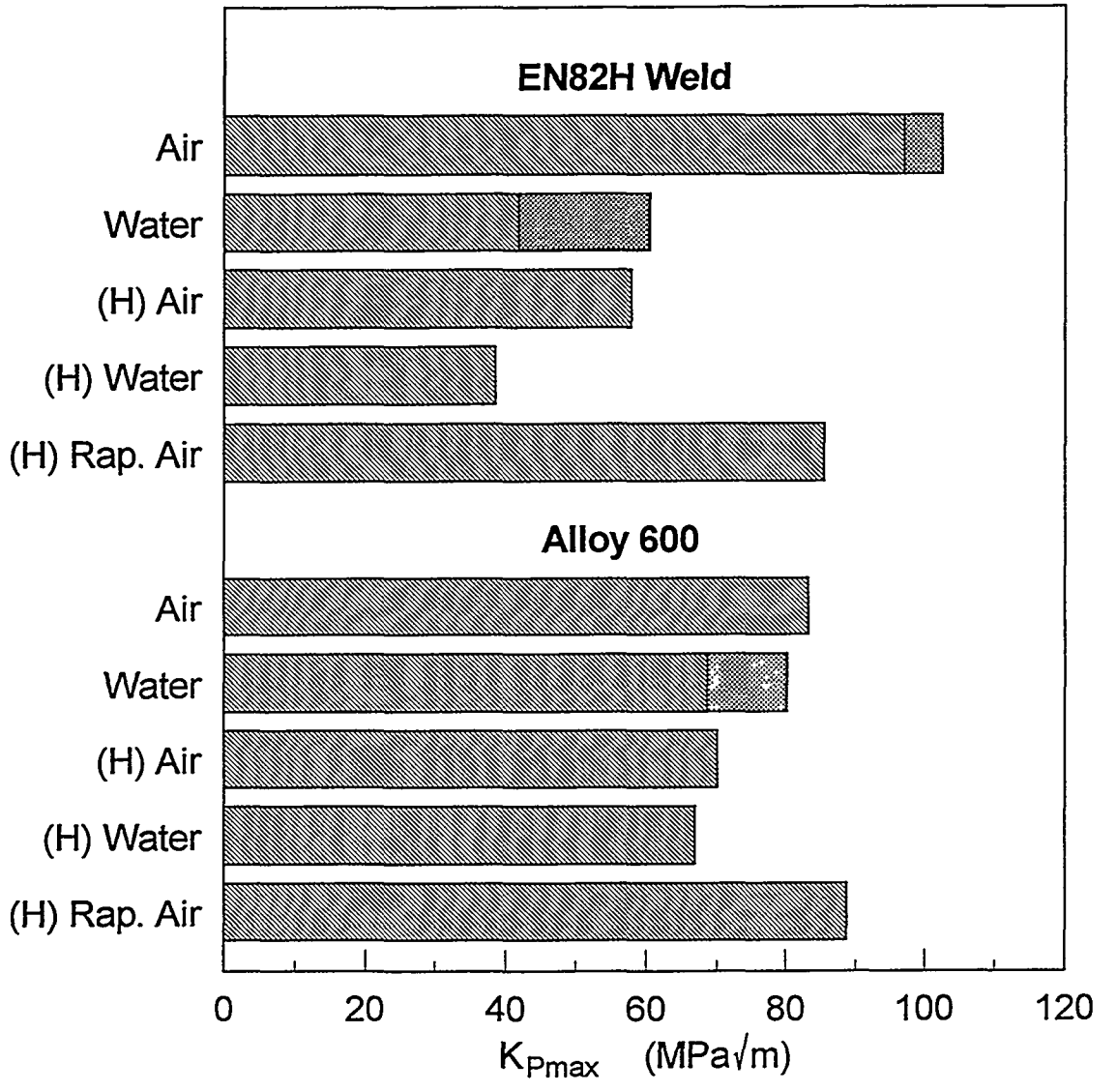

Figure 12. K_{Pmax} values for EN82H weld and Alloy 600. Non-precharged specimens were tested in 130°F air or water, while hydrogen-precharged [H] specimens were tested in 75°F air or water. The short test times for the rapid loading tests [Rap], where maximum load was reached in 1 to 3 seconds, preclude hydrogen from diffusing to the crack tip; hence, bulk hydrogen levels control fracture behavior. Crosshatching represents a range of K_{Pmax} values.

KPmax12

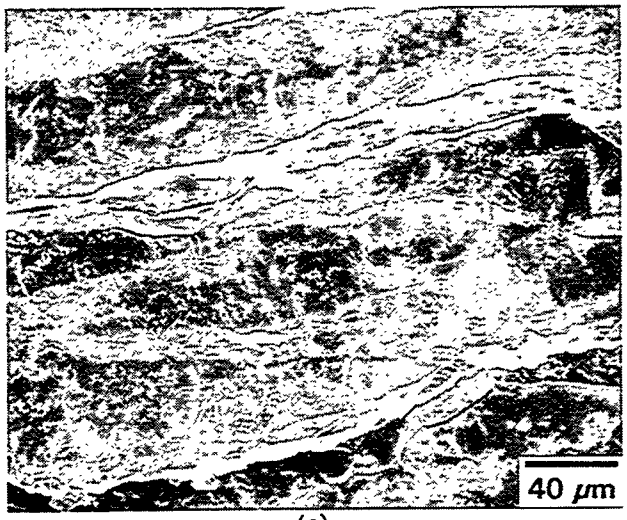

(a)

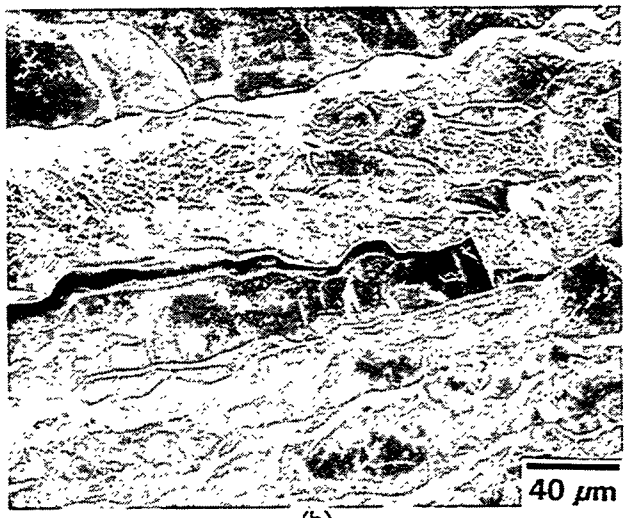

(b)

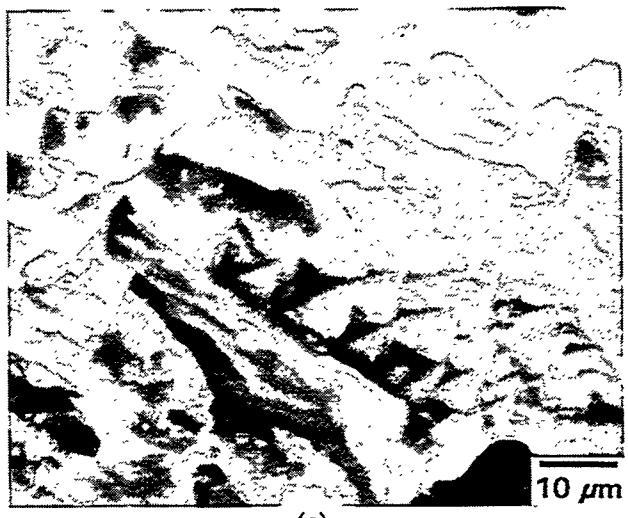

(c)

82FR5.cdr

Figure 13. SEM fractographs of hydrogen-precharged EN82H weld. (a) Intergranular cracking. (b) Intergranular fracture (top and bottom half) surrounding transgranular island with facets and poorly defined dimples. (c) Crystallographic facets within transgranular region.

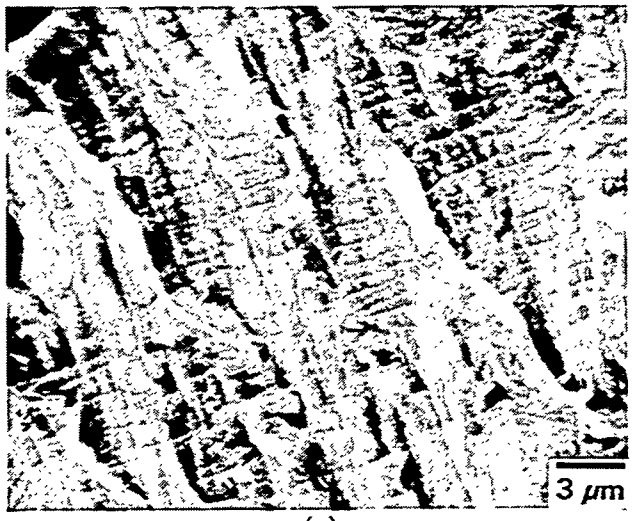

(a)

(b)

Figure 14. SEM fractographs of EN82H welds showing planar slip offsets superimposed on transgranular facets. (a) Non-precharged specimen tested in 54°C water. (b) Hydrogen-precharged specimen tested in water.

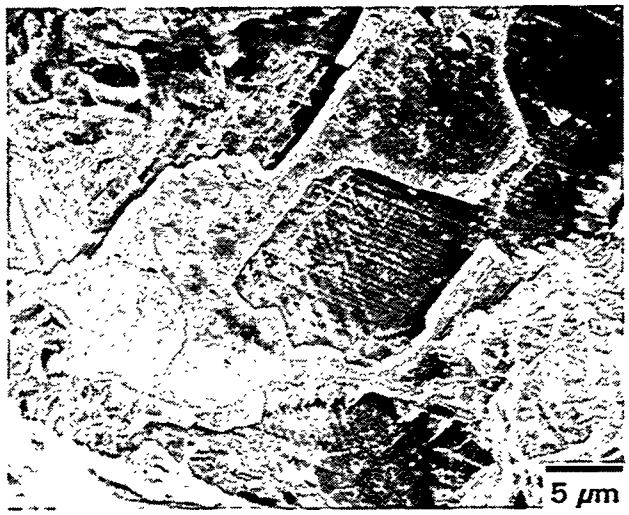

Figure 15. Fracture surface of hydrogen-precharged Alloy 600 showing slip offsets superimposed on crystallographic facets.